



Performance of layered birnessite-type manganese oxide in the thermal-catalytic degradation of polyamide 6

Erdal Eren ^{*}, Murat Guney, Bilge Eren, Huseyin Gumus

Bilecik Seyh Edebali University, Faculty of Science and Arts, Department of Chemistry, 11210 Bilecik, Turkey

ARTICLE INFO

Article history:

Received 8 August 2012

Received in revised form 3 December 2012

Accepted 7 December 2012

Available online 16 December 2012

Keywords:

Polyamide 6

Catalytic degradation

Birnessite

Layered oxides

Oxidation

ABSTRACT

The nature and the extent of degradation of polyamide 6 (PA6) in the presence of layered birnessite-type manganese oxide (LMO) were analysed by thermogravimetric analysis under static air atmosphere at several heating rates between 5 °C/min and 20 °C/min. The samples were characterized using infrared (IR) spectroscopy, X-ray diffraction (XRD), scanning electron microscopy (SEM), N₂ gas adsorption–desorption and thermal analysis (TA) techniques. XRD and DTA results for LMO showed that the oxidative transformation of MnO₂ was occurred on heating from 300 °C to 500 °C. The IR spectra of Mn–O band proved the covalent character of oxygen bonding to the metal ions of the surface. The addition of LMO caused the change in the crystalline phase of PA6 from predominantly α to largely γ phase. The activation energy for degradation estimated by Kissinger method for PA6 and 10 wt.% LMO/PA6 composite were found to be 213 and 118 kJ/mol in static air atmosphere, respectively. The experimental results revealed that the addition of 10 wt.% LMO decreased the thermal stability in static air of PA6 by about 80 °C.

© 2012 Elsevier B.V. All rights reserved.

1. Introduction

Thermal degradation of polymers have drawn attention because of their importance in the conversion of waste polymers to useful chemical or fuels [1–3]. Pure thermal degradation of waste polymers requires high temperatures and results in a wide variety of products. The addition of a catalyst improves the quality of products obtained from decomposition of polymers and reduces the temperature of decomposition [4,5].

Polyamides (PA) are an important group of the thermoplastic polycondensates. The amide group can be obtained by polymerization of lactams or by condensation of diamines with dicarboxilic acids. The thermal degradation of polyamides were studied systematically in the past [6,7]. The mechanistic studies about the thermal degradation products of polyamides showed that the thermal degradation was initiated by hydrogen abstraction from the methyl-group adjacent to the nitrogen atom and propagated by oxidation of the formed macroradical [6,7]. Karstens and Rossbach [6,7] proposed a detailed degradation scheme starting with oxygen attack at the N-vicinal methylene group (Scheme 1). The mechanism was supported by many other authors [8–12].

Manganese oxides are reported to be among the most efficient oxide solids for catalytic oxidation reactions such as the selective

catalytic reduction of NO_x with NH₃ [13], the catalytic decomposition of ozone [14], the catalytic combustion of volatile organic compounds [15] and catalytic decomposition of polymers [16–18]. This behavior is attributed to the variable electronic structure and oxidation state in a variety of compounds (MnO₂, Mn₂O₃ and Mn₃O₄), which shows good redox properties.

Solid acid catalysts, such as manganese oxides, promote hydrogen transfer reactions due to the presence of many acid sites. A careful analysis of the existing literature indicates that not many studies have been conducted at understanding the catalytic thermal degradation pathway of PA6 using manganese oxides. The role of manganese oxide catalysts in oxidation reactions prompted us to study the effect of this catalysts on PA6 degradation reactions. Taking into account this background, layered birnessite-type manganese oxide (LMO) was synthesized and evaluated in the catalytic thermal degradation of PA6. Infrared (IR) decomposition studies of PA6 on LMO were performed to get a better insight in the degradation mechanism.

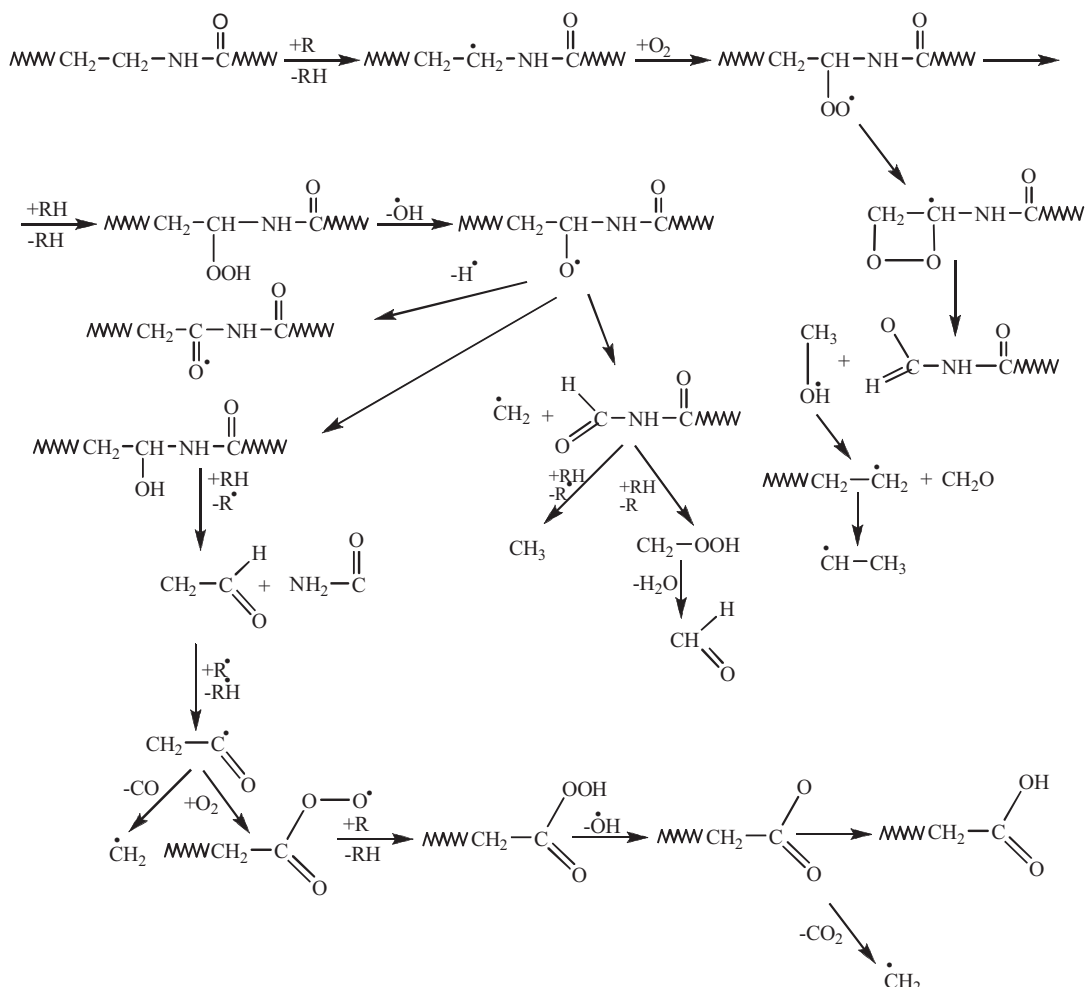
2. Experimental

2.1. Materials and sample preparation

PA6 pellets used in this study were obtained commercially from Resinex. Other chemicals were of >99.9% purity or of analytical grade, and purchased from Sigma–Aldrich Co. and used without

* Corresponding author. Tel.: +90 228 214 1164; fax: +90 228 214 1162.

E-mail address: erdal.eren@bilecik.edu.tr (E. Eren).



Scheme 1. Thermo-oxidation route according to Karstens and Rossbach [6,7].

further purification. Double distilled water was used throughout the experiments.

LMO was prepared according to the redox method described in [19]. Accordingly, firstly 2 M (mol/L) H_2O_2 and 0.6 M (mol/L) NaOH solutions was mixed and stirred in glass beaker. The molar ratio of NaOH/ H_2O_2 was adjusted as 0.18. After that, immediately manganese solution was poured in to the mixture. During the addition highly vigorous reaction accurred. This reaction continued until to run out all of the manganese solution. After completion of bubbles formation, black precipitate was filtered. Obtained soil was put in to the teflon lined autoclave and waited at 140 °C for 16 h in 2 M sodium hydroxide alkaline solution. As a final opretation obtained grey precipitate was filtered and washed with deionized water until to obtain neutralization. Several IR absorption bands were observed at 3412, 1633, 1384, 1066, 622, 602 and 513 cm^{-1} , respectively. Two strong IR bands could be observed around 513 and 602 cm^{-1} , in good agreement with the IR characteristic bands of birnessites [20–24]. The surface area was calculated by the BET (Brunauer–Emmett–Teller) method. The BET surface area (34.24 m^2/g), external surface area (28.56 m^2/g), micropores surface area (5.68 m^2/g), total pore volume (0.169 cm^3/g) and average pore diameter (19.79 nm) results obtained by applying the BET equation to N_2 adsorption at 77 K and Barret–Joymer–Halenda (BJH) equation to N_2 adsorption at 77 K.

2.2. Characterization techniques

Infrared (IR) spectra of the LMO samples were recorded in the region 4000–450 cm⁻¹ on a Spectrum-100 FTIR spectrometer. The thermal gravimetric (TG) and differential thermal analyses (DTA) curves were obtained using a PRIS Diamond TG/DTG apparatus under highly pure nitrogen atmosphere. A Tri Star 3000 (Micromeritics, USA) surface analyzer was also used to measure the nitrogen adsorption isotherm at 77 K in the range of relative pressure 10⁻⁶–1. The XRD analysis data from the samples were collected using a Rigaku, Miniflex ZD13113 (Japan) diffractometer with Cu K α radiation (Ni filter). Surface morphology was studied using a ZEISS Ultraplus model field emission scanning electron microscopy (SEM).

2.3. Thermal degradation of LMO/PA6 composite

The LMO/PA6 composite was prepared by dissolving stoichiometric amounts of PA6 and LMO in formic acid. The mixture was heated at 40 °C until complete dissolution was achieved. The solution was then cast onto a glass substrate followed by a slow evaporation of the formic acid in a fume hood, then in a vacuum oven at room temperature for 48 h. The thermal decomposition studies in the TGA were performed over a temperature range of

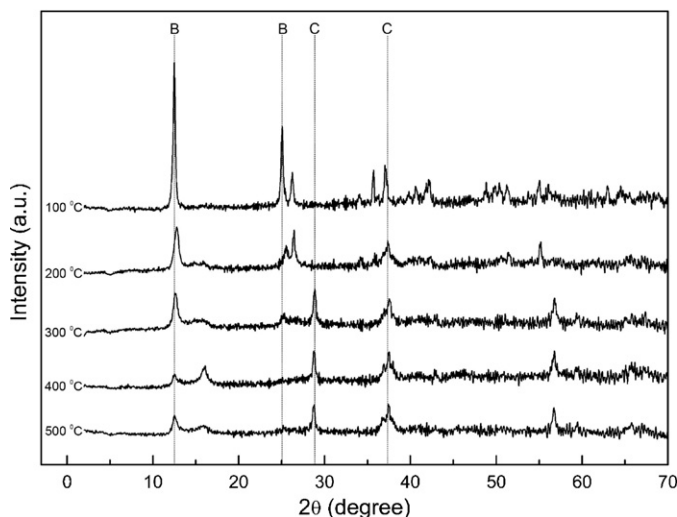


Fig. 1. XRD patterns of the LMO sample heated at various temperatures for 20 min. B, birnessite; C, cryptomelane.

50–800 °C under both static air environment at different heating rates of 5, 10, 20, 30 and 40 °C/min.

3. Results and discussion

3.1. Material characterisation

XRD and SEM techniques were used to study the morphology of the LMO/PA6 composite and how the MBO layers were distributed within the PA6. The XRD patterns obtained for raw MBO and LMO/PA6 composite samples, respectively, were presented in Figs. 1 and 2. The two peaks at 2θ values of 12.48° ($d_{001} = 7.08 \text{ \AA}$) and 25.30° ($d_{002} = 3.55 \text{ \AA}$) corresponded to 001 and 002 basal reflections of LMO, respectively, indicating an excellent agreement with other synthetic layered manganese oxides [25–28]. These peaks also point out the separation of the sheets of MnO_6 octahedral. The XRD pattern of LMO heated at 200°C revealed the presence of a mixture of two phases having basal spacing of 6.92 and 5.60 \AA , which were originated by normal and dehydrated birnessite, respectively. This result showed that the dehydration of the crystal water did not cause damage to the birnessite structure. At

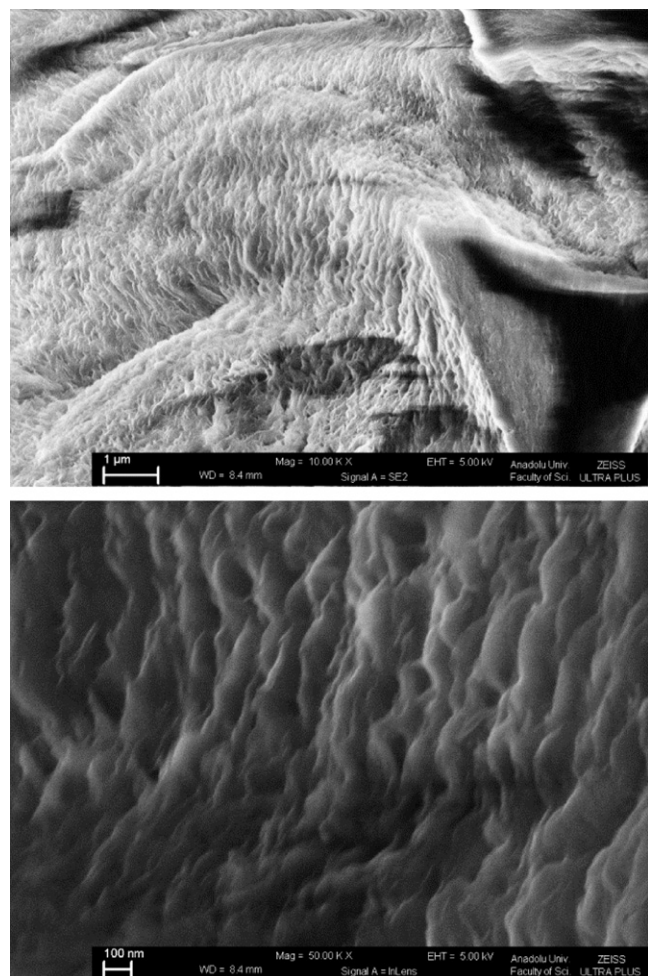


Fig. 3. The SEM images of 10 wt.% LMO/PA6 at different magnifications.

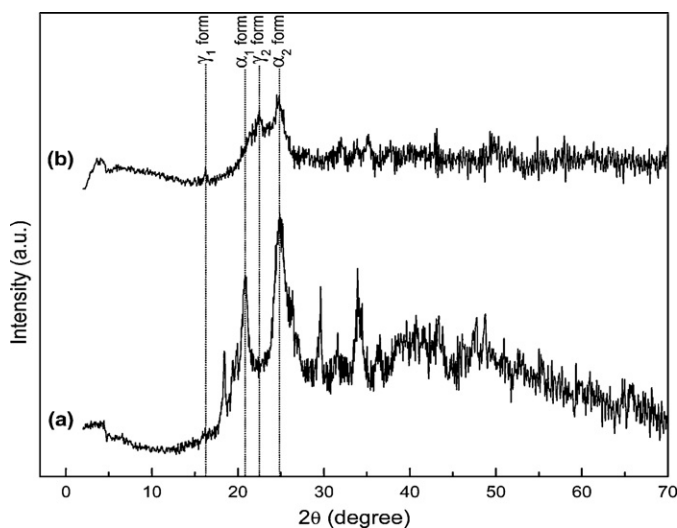


Fig. 2. XRD patterns of (a) 10 wt.% LMO/PA6 and (b) 10 wt.% LMO/PA6 heated at 300°C .

300°C , cryptomelane began to form, indicating the transformation from the layered structure to tunnel structure. The X-ray diffraction patterns of these two families of compounds were clearly distinguished by their characteristic Bragg diffractions at 12.54° and 24.95° for the LMO, and 28.97° and 37.52° for the cryptomelane [29,30]. The intensity of cryptomelane peaks also increased with increasing the calcination temperature.

The appearance of the new peak at $2\theta = 4.05^\circ$ with the disappearance of the (001) peak at $2\theta = 12.48^\circ$ and the increase in d-spacing indicated the formation of a nanocomposite structure with the intercalation of PA6 chains in the gallery of the MBO layers (Fig. 2). Aiming to prove intercalated PA6 chains between the LMO layers, the LMO/PA6 composite was heated in a reducing atmosphere up to 300°C . This heated sample presented a basal spacing of 13 \AA , confirming polymer intercalation since the LMO layer structure in the heated composite would collapse to a basal spacing of 7.08 \AA in the absence of polymer residues between layers.

The PA 6 has multi-crystalline forms and usually exhibits a more stable α -form rather than the γ -form [31–33]. The α_1 peak in XRD pattern of PA6 arises from the distance between hydrogen-bonded chains which is the diffraction of hydrogen bonded sheets, and the α_2 peak arises from the separation of the hydrogen bond sheets [31–33]. The LMO/PA6 composite showed the presence of two α -crystalline peaks at 20.79° (α_1 -form) and 25.07° (α_2 -form) with no indication of γ -forms at 16.25° (γ_1 -form) and 22.55° (γ_2 -form) (Fig. 2b). At 300°C , disappearing α_1 -form peak indicated that the LMO disturbed the arrangement of hydrogen bonded sheets of the α -form. This result showed that the closeness of the LMO layers

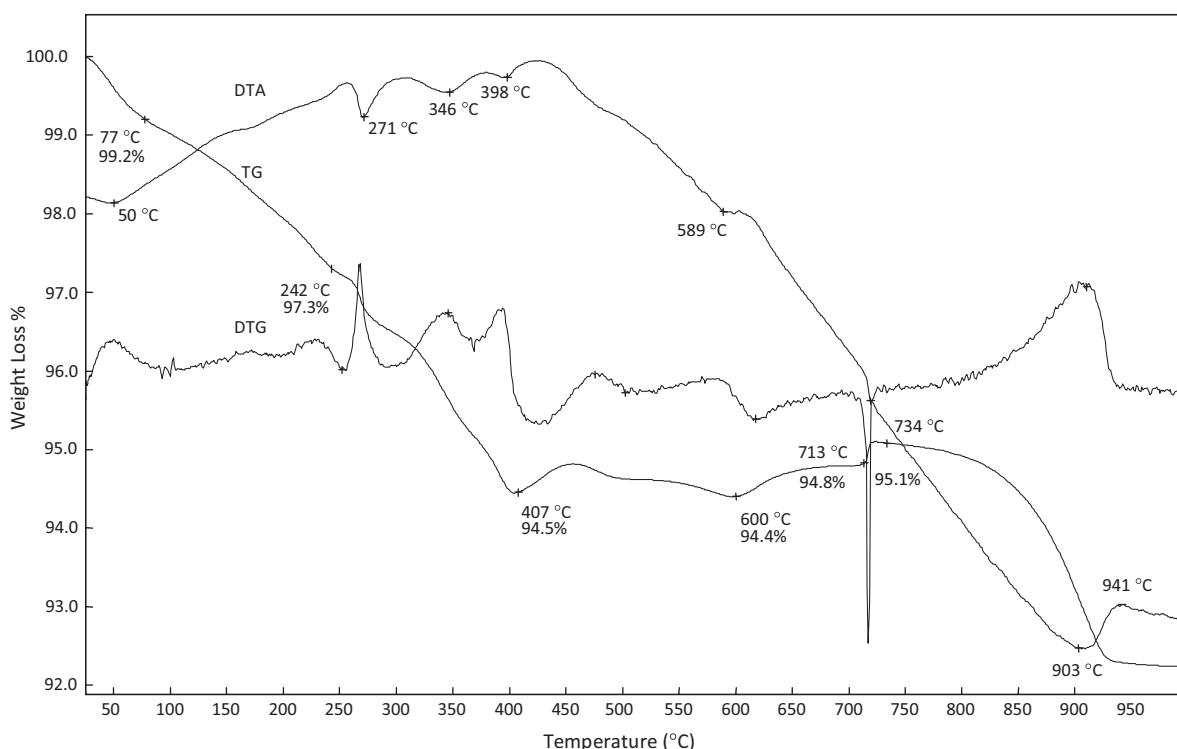


Fig. 4. Thermal analysis curves of the LMO sample.

led to the conformation changes of chains, limiting the formation of hydrogen bonded sheets of the α -form. This result was also supported the appearance of the new peaks indicated the γ_1 - and γ_2 -form at 2θ values of 16.25° and 22.55° , respectively.

SEM images did not exhibit birnessite domains at the maximum possible magnification, which means birnessite layers were distributed well in the polyamide matrix (Fig. 3). The absence of LMO particles indicated that the agglomerate was broken down to a size that cannot be seen at this magnifications. The image of 10 wt.% LMO/PA6 (Fig. 3) exhibited an oriented type of morphology which could be due to a highly intercalated state manipulating the film formation along with the birnessite layers.

The thermal stability of LMO sample was investigated by TG and DTA (Fig. 4). The curve related to the LMO exhibited mass losses by 2.8 and 4.6% in temperature ranges 20–200 and 200–1000 °C, respectively (Fig. 4). The endothermic peak at 55 °C was assigned to evaporation of adsorbed water. The DTA curve had a broad endothermic peaks at 271, 346 and 398 °C. This is probably due to the departure of oxygen corresponding to its reduction into Mn_2O_3 [34]. The loss of 3.6% at 200–400 °C was attributed to dissociatively chemisorbed water, strongly bound micropore water and hydroxyl groups in the interior of the lattice [35]. The weight gained in the temperature range of 703–721 °C was showed the partial reduction of Mn(IV) to Mn(III) and subsequent oxidation of Mn(III) [18]. The endothermic peak at about 903 °C in DTA curve indicates the transformation of LMO and Mn_2O_3 to Mn_3O_4 [34].

3.2. Thermal degradation behavior of LMO/PA6 composite

The thermo-oxidative degradation activation energy of sample containing 10 wt.% of LMO was calculated by Kissinger method [36] according to the TG data, which were measured under air at different heating rates: 2.5, 5, 10, 15, and 20 °C/min. The activation energy for PA6 and LMO/PA6 composite was calculated from the linear dependence of the $\ln(\beta/T_{\max}^2)$ versus $1/T_{\max}$ plot (not shown) for various heating rates according to Eq. (1).

$$\ln \left(\frac{\beta}{T_{\max}^2} \right) = \left\{ \ln \frac{AR}{E_a} \right\} - \frac{E_a}{RT_{\max}} \quad (1)$$

In the above equation, A is the pre-exponential factor, E_a is the apparent activation energy of the degradation reaction, R is the universal gas constant, β is the heating rate. The activation energy was calculated from the T_{\max} , the temperature at which the maximum degradation occurs for different heating rates by assuming that weight loss percentage at T_{\max} is constant. E_a values calculated by this method are listed in Table 1.

The E_a of PA6 was 213 kJ/mol and decreased to 118 kJ/mol after loading of 10 wt.% LMO content into PA6 matrix under static air atmosphere. The thermal properties of LMO/PA6 samples containing 2.5, 5, 10 and 15 wt.% LMO and neat PA6 were also investigated by using TG under static air atmosphere at a rate of heating of 10 °C/min (Fig. 5). In general, the TG curves of PA6 and LMO/PA6 showed three stages of weight loss. In the first stage, an initial

Table 1
 T_{\max} and activation energy values of PA 6 and LMO/PA6 samples.

LMO content (wt.%)	β (°C/min)						E_a (kJ/mol)	R^2
		5	10	20	30	40		
–	T_{\max} (°C)	477	482	487	505	518	213	0.900
2.5	T_{\max} (°C)	391	425	432	443	462	118	0.933
5	T_{\max} (°C)	395	430	432	451	462	121	0.922
10	T_{\max} (°C)	382	386	422	440	460	87	0.927
15	T_{\max} (°C)	378	380	420	437	454	85	0.911

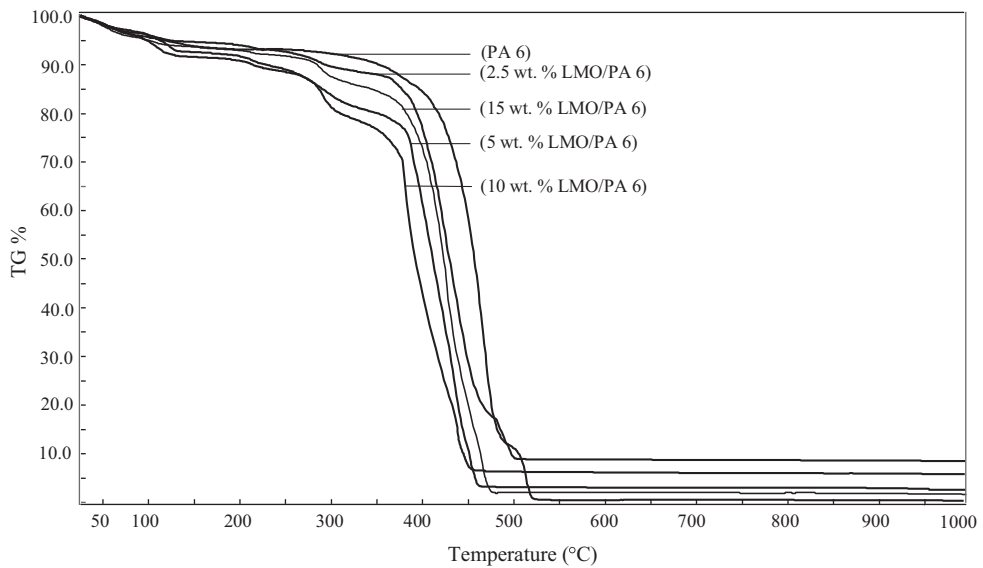


Fig. 5. TG curves of PA 6 and 10 wt.% LMO-PA 6 composite obtained at a heating rate of 10 °C/min in static air atmosphere.

weight loss of 1–5% occurred in the temperature range 100–200 °C. The second stage corresponded to steep fall (200–470 °C) in the TG curve. The weight loss in this stage for PA6 and LMO/PA6 was about 49.2 and 81.6%, respectively. In the third stage, above 500 °C,

the weight loss in the TG curves were steady. The temperature at the maximum decomposition rate, T_{\max} , of the LMO/PA6 composite containing 2.5 wt.% of LMO was 430 °C. This value decreased to 425, 386 and 380 °C for 5, 10 and 15 wt.% of LMO, respectively.

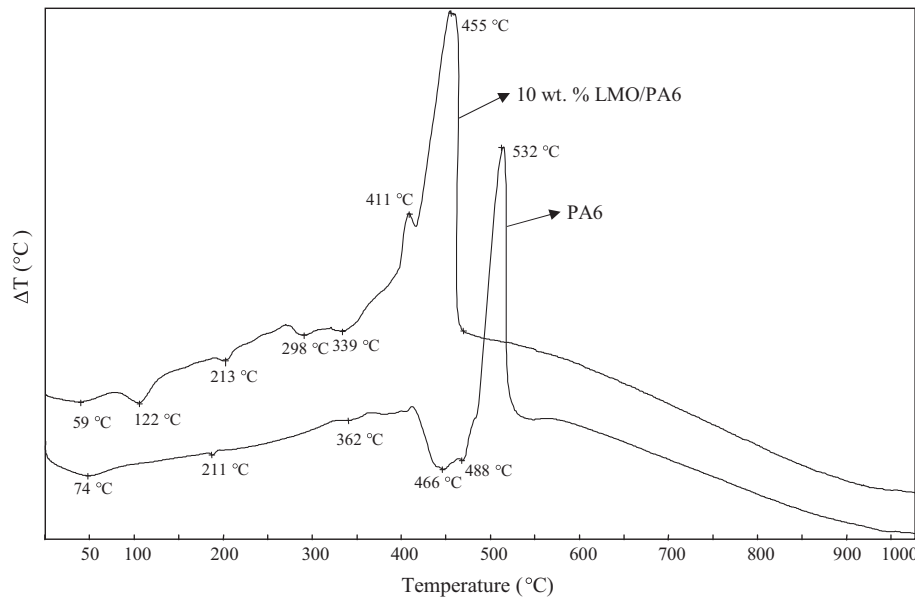


Fig. 6. DTA curves of PA6 and 10 wt.% LMO/PA6 composite in static air atmosphere with a heating rate of 10 °C/min.

Table 2

TG/DTA characteristics of PA6 and 10 wt.% LMO/PA6.

Material	Thermaldegradation step	$T_{\text{onset}}(^\circ\text{C})$	$T_{\text{peak}}(^\circ\text{C})$	$T_{\text{endset}}(^\circ\text{C})$	W (%)	Residue	DTA characteristic
PA6	I	30	74	110	5.0	0	Endothermic
	II	210	211	213	0.2		Endothermic
	III	355	362	370	4.8		Endothermic
	IV	430	466(488)	492	39.2		Endothermic
	V	492	532	570	50.8		Exothermic
LMO/PA6	I	30	59	80	3.8	8.1	Endothermic
	II	105	122	162	0.8		Endothermic
	III	210	213	226	2.1		Endothermic
	IV	280	298	320	1.6		Endothermic
	V	330	339	375	4.8		Endothermic
	VI	380	411(455)	469	68.5		Exothermic

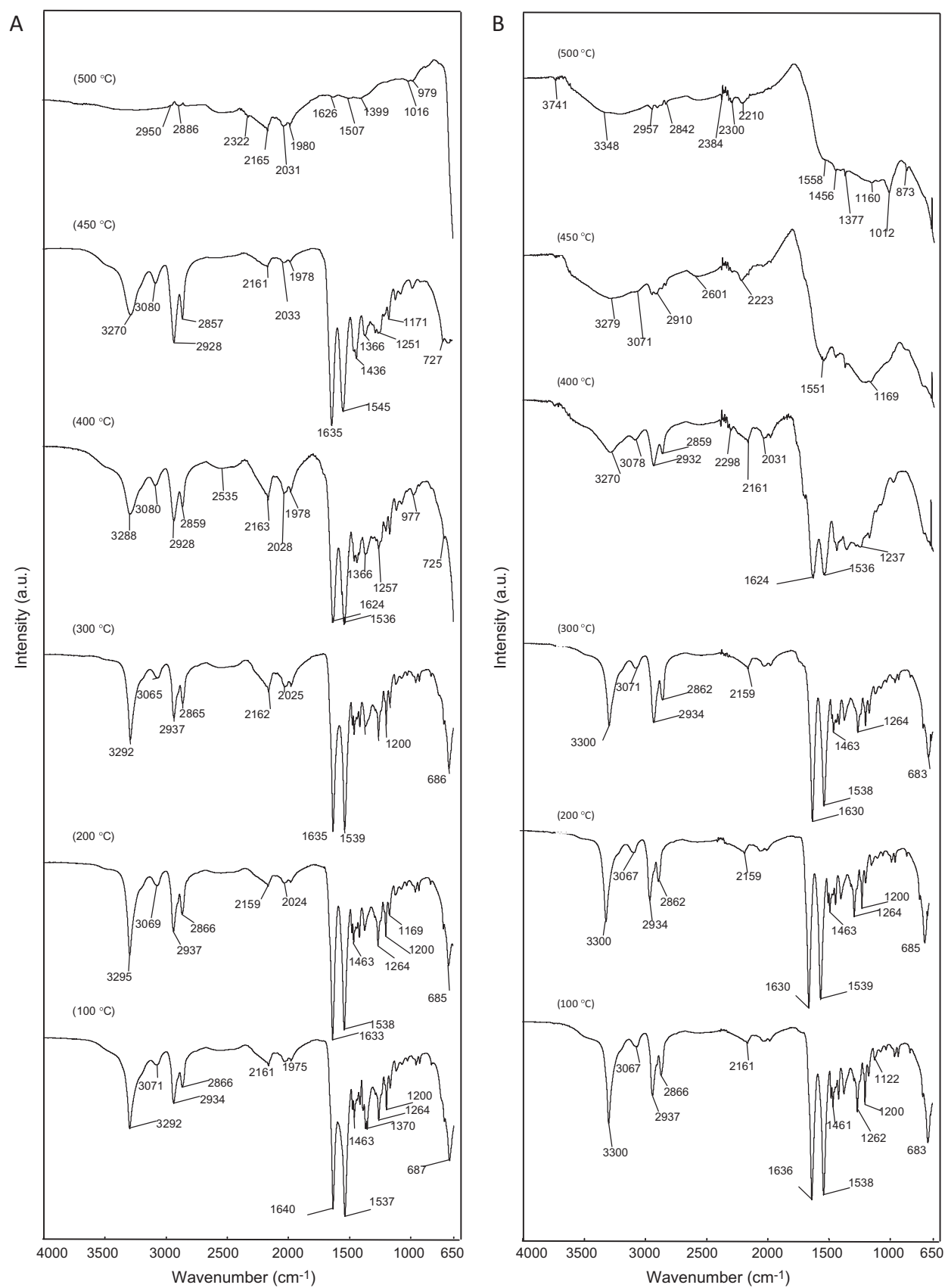
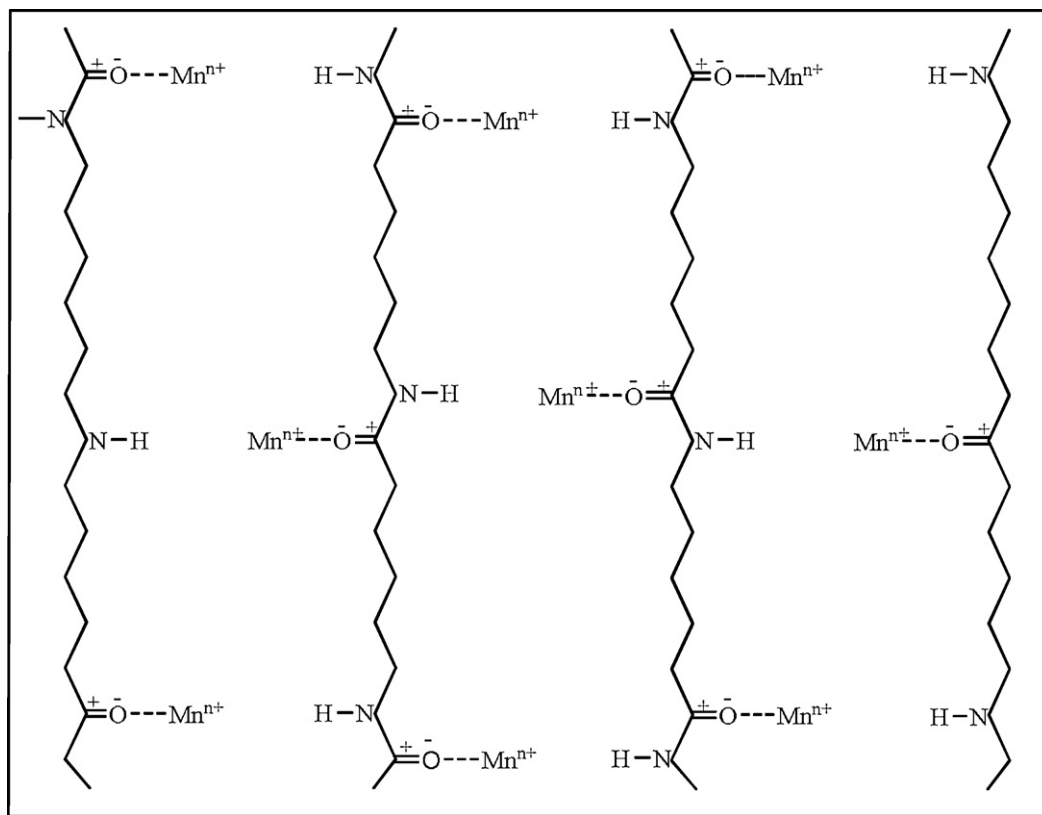


Fig. 7. IR spectra at different temperatures for PA 6 (A) and 10 wt.% LMO-PA 6 composite (B) under air.



Scheme 2. Breaking of the hydrogen bonds between PA6 chains after LMO addition.

These results implied that the thermal stability of PA6 significantly decreased as the weight percentage of LMO increased. When 50% weight loss was chosen as a point of comparison, the decomposition temperatures were 436 and 407 °C for PA6 and 10 wt.% LMO/PA6 samples, respectively. The percentage weight loss of PA6 increased from 61.1% at 470 °C to 85% at 500 °C. Under the same range of temperature change, a small increase of weight loss (81.6 versus 83%) was observed for LMO/PA6. This suggested that catalytic thermal decomposition of PA6 in the presence of LMO can be carried out at a lower temperature to achieve the same decomposition results.

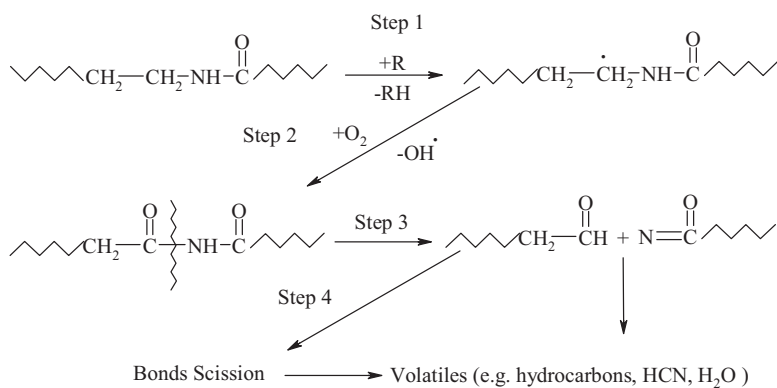
The DTA curves were recorded in static air atmosphere in order to obtain more information about the thermal transitions occurred. The DTA curves for neat PA6 and 10 wt.% LMO/PA6 samples were shown in Fig. 6. For better oversight of data attained from thermal studies, the following characteristics of investigated samples were represented in Table 2: initial temperature at which thermal decomposition started T_{onset} , temperature at which maximal degradation was registered T_{peak} and temperature at which investigated process finished T_{endset} besides, the percentage of mass loss in each step W%. As can be seen from results represented in Figs. 5 and 6, prepared LMO/PA6 composite, comparing to neat PA6, showed the same thermal behavior. In the first stage for LMO/PA6 composite, the endothermic peak at 122 °C was ascribed to evaporation of remained solvents. In the second degradation step of LMO/PA6 composite, TG curve had three endothermic peaks at 213, 298 and 339 °C and exothermic peaks at 411 and 455 °C (Fig. 6). In this stage, the first peak at 213 °C corresponded to melting of crystalline PA 6. The exothermic peak of oxidative reaction observed at 455 °C for LMO/PA6 was assigned to the combustion of the residues. As given in Section 3.1, three endothermic peaks were observed at 271, 346 and 398 °C due to partial transformation of the MnO_2 to Mn_2O_3 together with release of oxygen gas. Thus, the decreased thermal stability of PA6 was in the presence of the LMO was attributed the accelerated chain oxidation

arising from oxygen released from the partial transformation of the MnO_2 to Mn_2O_3 .

3.3. IR characterization of LMO/PA6 composite

In order to understand the thermal degradation process of PA6 and LMO/PA6 in air, IR spectra were recorded in the range of 4000–650 cm^{-1} at various temperatures (Fig. 4). The IR spectra of LMO/PA6 are different to that of PA6 between 100 and 600 °C. In the 100 °C spectrum of the PA6 sample, important polyamide bands were observed at 3292 (NH stretching), 3076 (N–H in-plane bending), 1638 (Amide I), 1538 (Amide II), 2937 (CH₂ stretching) and 2866 cm^{-1} (CH₂ stretching) (Fig. 7).

N–H stretching and Amide I bands strongly depend on hydrogen bonding interactions between the PA6 chains. The amide group is potentially a bi-functional electron donor with 2 sp^2 “lone pairs” at the oxygen atom and a 2p_z “lone pair” at the nitrogen atom, and therefore it has two possible electron-donating sites to coordinate with the manganese cations. Overlap of 2p_z orbitals of the oxygen, carbon, and nitrogen atoms in the planar amide group would reduce the electron density on the nitrogen atom, and favor the coordination of the manganese ion with the carbonyl oxygen atom. Manganese cation coordination leads to breaking of the hydrogen bonds between PA6 chains (Scheme 2). Since manganese cation forms a complex with the C=O group, the N–H bond is free. Therefore the N–H vibrational band is shifted to higher frequency, while the C=O vibrational band is shifted to lower frequency due to the reduction of bond order. The C=O band is shifted from 1640 cm^{-1} to 1635 cm^{-1} in the complex, while the N–H band at 3292 cm^{-1} is shifted to 3300 cm^{-1} in the LMO/PA6. These bands remained sharp and distinct up to 400 °C. In the infrared spectrum of the LMO/PA6 at 400 °C, important changes for these peaks were observed. First, the C=O band shifted from 1635 cm^{-1} to 1624 cm^{-1} and the N–H band at 3288 cm^{-1} shifted to 3300 cm^{-1} . Second, the relative



Scheme 3. Thermal degradation mechanism of PA 6 in the presence of oxygen according to Karstens and Rossbach [6,7] (the intermediates as drawn do not imply a concerted mechanism, but show the possible rearrangement of atoms and bonds).

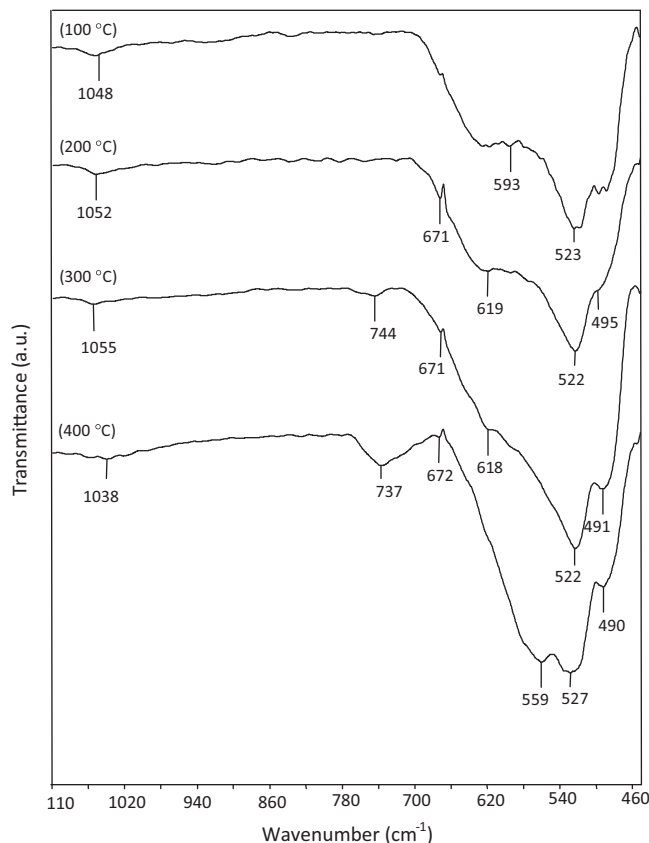


Fig. 8. IR spectra of the LMO between 100 and 400 °C.

intensities of these bands greatly diminished. In the infrared spectrum of the LMO/PA6 at 450 °C and higher temperatures, all the amide related peaks and aliphatic CH_2 stretching peaks disappeared.

3.4. Thermal degradation mechanism of PA6

Some recent studies have provided evidences about mechanism of thermal decomposition of PA6 [6–12]. In addition to these proofs, other experimental evidences must be considered. They are follows: (1) the IR spectra of LMO sample at different temperatures in the range from 1100 to 450 cm^{-1} were shown in Fig. 8. The bands in the region between 450 and 750 cm^{-1} were assigned to Mn–O vibrations [37–42]. The band located at 523 cm^{-1} were ascribed to the Mn–O bending vibration of $[\text{MnO}_6]$ octahedra in LMO sample

[38,42]. After heating at 400 °C, the IR band at 523 cm^{-1} shifted to lower frequency and splitted into two bands at 559 and 527 cm^{-1} . This was an evidence for the decrease of the surface Mn–O bond strength. The increase of the width of the same band in LMO, i.e. the growth in its integral intensity was another confirmation of the fact that the decrease of the surface Mn–O bond strength. This results indicated that heating process influenced the mobility of the reacting oxygen, contributing to activity of LMO in thermal degradation process. (2) The XRD signal intensities and the signal/background ratios of LMO in the composite heated at 400 °C greatly decreased (Supporting Information, Figure S1 and Fig. 2). It suggested that the crystallization degree of the LMO catalyst significantly decreased. It might be due to the fact that the manganese and oxygen ions in the LMO moved off their lattice positions in the course of PA6 catalytic reaction [43]. The results implied that the Mn–O bonds in the MnO_2 partly were cleaved during PA6 oxidation. (Figure S1 and Fig. 2). In view of the fact that pointed above, it is evident that LMO enhanced the thermo-oxidative degradation of PA6. Based on our results and on other similar investigation [6,7], a mechanism concerning the oxidation by thermal degradation of PA6 was presented in Scheme 3.

Supplementary material related to this article found, in the online version, at <http://dx.doi.org/10.1016/j.apcatb.2012.12.006>.

4. Conclusion

The results revealed that LMO could act as an effective catalyst for reducing the degradation temperature of PA6. The onset and end-point temperatures of the initial stage TGA curve for the LMO/PA6 composites were decreased. It was clearly observed that the activation energy of the thermal degradation for the LMO/PA6 composite is less than that of the neat PA6. During catalytic degradation with LMO/PA6 in air atmosphere, LMO favored hydrogen transfer reactions due to the presence of many acid sites and therefore recombination of macromolecular hydrocarbon radicals may be suppressed. The activation of PA6 decomposition by manganese oxide can also be attributed to the reduction of Mn(IV) to Mn(III) form accompanied by the evolution of oxygen. LMO showed an exothermic effects between 300 and 500 °C in its DTA curve, which is due to a partial transformation of the layered structure to cryptomelane (with simultaneous oxygen evolution), which was identified by XRD in the sample on heating from 300 to 500 °C. The IR spectra of Mn–O band proved the covalent character of oxygen bonding to the metal ions of the surface, which in its turn justified the assumption of high activity of the LMO in reaction of thermal decomposition. The TG curves of PA6 and LMO/PA6 showed drastic degradation in the temperature range 300–500 °C. After heating at 300 °C, the addition of LMO favoured the

formation of the γ crystalline phase, due to the interaction between LMO compounds layers and PA6 chains.

References

- [1] A. Durmuş, S.N. Koç, G.S. Pozan, A. Kaşgöz, *Applied Catalysis B: Environmental* 61 (2005) 316–322.
- [2] Y.-H. Lin, M.-H. Yang, *Applied Catalysis B: Environmental* 69 (2007) 145–153.
- [3] F.J. Passamonti, U. Sedran, *Applied Catalysis B: Environmental* 125 (2012) 499–506.
- [4] N.S. Akpanudoh, K. Gobin, G. Manos, *Journal of Molecular Catalysis A: Chemical* 235 (2005) 67–73.
- [5] N. Miskolczi, L. Bartha, Gy Deák, *Polymer Degradation and Stability* 91 (2006) 517–526.
- [6] T. Karstens, V. Rossbach, *Makromolekulare Chemie* 190 (1989) 3033–3053.
- [7] T. Karstens, Rossbach V. *Makromolekulare Chemie* 191 (1990) 757–771.
- [8] G. Ahlblad, D. Forsström, B. Stenberg, B. Terselius, T. Reitberger, L.-G. Svensson, *Polymer Degradation and Stability* 55 (1997) 287–293.
- [9] R. Li, X. Hu, *Polymer Degradation and Stability* 62 (1998) 523–528.
- [10] M. Gröning, M. Hakkarainen, *Journal of Chromatography A* 932 (2001) 1–11.
- [11] M.J. Oliveira, G. Botelho, *Polymer Degradation and Stability* 93 (2008) 139–146.
- [12] W. Dong, P. Gijssman, *Polymer Degradation and Stability* 95 (2010) 1054–1062.
- [13] X. Tang, J. Li, L. Sun, J. Hao, *Applied Catalysis B: Environmental* 99 (2010) 156–162.
- [14] Y. Dong, H. Yang, K. He, S. Song, A. Zhang, *Applied Catalysis B: Environmental* 85 (2009) 155–161.
- [15] S.C. Kim, W.G. Shim, *Applied Catalysis B: Environmental* 98 (2010) 180–185.
- [16] P. Zhang, L. Song, H. Lu, Y. Hu, W. Xing, J. Ni, J. Wang, *Polymer Degradation and Stability* 94 (2009) 201–207.
- [17] F. Rault, E. Pleyber, C. Campagne, M. Rochery, S. Giraud, S. Bourbigot, E. Devaux, *Polymer Degradation and Stability* 94 (2009) 955–964.
- [18] G. Liu, S. Liao, D. Zhu, J. Cui, W. Zhou, *Solid State Sciences* 13 (2011) 88–94.
- [19] X. Li, G. Pan, Y. Qin, T. Hu, Z. Wu, Y. Xie, *Journal of Colloid and Interface Science* 271 (2004) 35–40.
- [20] F. Li, J. Wu, Q. Qin, Z. Li, X. Huang, *Journal of Alloys and Compound* 492 (2010) 339–346.
- [21] U. Bentrup, A. Brückner, M. Richter, R. Fricke, *Applied Catalysis B: Environmental* 32 (2001) 229–241.
- [22] Q. Feng, K. Yanagisawa, N. Yamasaki, *Journal of Materials Science Letters* 16 (1997) 110–112.
- [23] L. Zhang, Z.-H. Liu, X. Tang, J. Wang, K. Ooi, *Materials Research Bulletin* 42 (2007) 1432–1439.
- [24] L. Kang, M. Zhang, Z.-H. Liu, K. Ooi, *Spectrochimica Acta A* 67 (2007) 864–869.
- [25] M. Nakayama, M. Shamoto, A. Kamimura, *Chemistry of Materials* 22 (2010) 5887–5894.
- [26] Y. Li, Y. Wu, *Nano Research* 2 (2009) 54–60.
- [27] M. Händel, T. Rennert, K.U. Totsche, *Geoderma* 193/194 (2013) 117–121.
- [28] Kh.S Abou-El-Sherbini, M.H. Askar, R. Schöllhorn, *Solid State Ionics* 150 (2002) 407–415.
- [29] D. Frías, S. Nousir, I. Barrio, M. Montes, T. López, M.A. Centeno, J.A. Odriozola, *Material Characteristics* 58 (2007) 776–781.
- [30] M.A. Cheney, R. Jose, A. Banerjee, P.K. Bhowmik, S. Qian, J.M. Okoh, *Journal of Nanomaterials* (2009) 1–8, 10.1155.
- [31] Z.-M. Wu, J.-Y. Wu, *Journal of Macromolecular Science: Physics B* 41 (2002) 17–31.
- [32] Z. Kadlecová, R. Puffr, J. Baldrian, P. Schmidt, J. Roda, J. Brožek, *European Polymer Journal* 44 (2008) 2798–2806.
- [33] T. McNally, W.R. Murphy, C.Y. Lew, R.J. Turner, G.P. Brennan, *Polymer* 44 (2003) 2761–2772.
- [34] L. Liu, Q. Feng, K. Yanagisawa, G. Bignall, T. Hashida, *Journal of Materials Science* 37 (2002) 1315–1320.
- [35] H. Malankar, S.S. Umare, K. Singh, M. Sharma, *Journal of Solid State Electrochemistry* 14 (2010) 71–82.
- [36] H.E. Kissinger, *Analytical Chemistry* 29 (11) (1957) 1702–1706.
- [37] J. Yuan, Z.-H. Liu, S. Qiao, X. Ma, N. Xu, *Journal of Power Sources* 189 (2009) 1278–1283.
- [38] K. Ramalingam, T. Kamatchi, P.A. Sumod, *Transition Metal Chemistry* 31 (2006) 429–433.
- [39] S. Liang, F. Teng, G. Bulgan, R. Zong, Y. Zhu, *Journal of Physical Chemistry A* 112 (2008) 5307–5315.
- [40] L. Li, Y. Pan, L. Chen, G. Li, *Journal of Solid State Chemistry* 180 (2007) 2896–2904.
- [41] L. Kang, M. Zhang, Z.-H. Liu, K. Ooi, *Spectrochimica Acta A* 67 (2007) 864–869.
- [42] C.M. Julien, M. Massot, C. Poinsignon, *Spectrochimica Acta Part A* 60 (2004) 689–700.
- [43] St. Christoskova, M. Stoyanova, *Journal of Hazardous Materials* 165 (2009) 690–695.